

PAPER • OPEN ACCESS

Study on high-strength high-N austenitic stainless steel prepared by spark plasma sintering

To cite this article: Ling Hu *et al* 2021 *J. Phys.: Conf. Ser.* **2044** 012041

View the [article online](#) for updates and enhancements.

You may also like

- [Laser Cladded High ChromiumNitrogen Alloys on Carbon Steel](#)
ChongCheng Huang, WenTa Tsai and Ju Tung Lee
- [Temperature influence on mechanical properties of chromium nitride thin films](#)
F M erdean, V V Merie, G Negrea et al.
- [Adhesion analysis for chromium nitride thin films deposited by reactive magnetron sputtering](#)
F M Rusu, V V Merie, I M Pintea et al.

ECS
The
Electrochemical
Society
Advancing solid state &
electrochemical science & technology

DISCOVER
how sustainability
intersects with
electrochemistry & solid
state science research

Study on high-strength high-N austenitic stainless steel prepared by spark plasma sintering

Ling Hu^{1,2,a}, Zhongmei Zhang^{2,b}, Liejun Li^{1,*}, Hanlin Peng^{3,c}, Jixiang Gao^{4,d}

¹School of Mechanical and Automotive Engineering, South China University of Technology, Guangzhou 510640, China

²Omat Advanced Materials Co., Ltd., Shaoguan 512029, China

³Guangdong Provincial Key Laboratory of Advanced Welding Technologies, China-Ukraine Institute of Welding, Guangdong Academy of Sciences, Guangzhou 510650, China

⁴School of Mechatronic Engineering, Guangdong Polytechnic Normal University, Guangzhou 510665, China

^aemail: ling.hu@omat.com.cn

^bemail: zm.zhang@omat.com.cn

^cemail: penghl@gwi.dg.cn

^demail: gaojx@gpnu.edu.cn

Corresponding author: *email: liliejun@scut.edu.cn

Abstract: A novel method consists of nitriding and spark plasma sintering was used to fabricate high nitrogen austenitic stainless steel (HNASS). The influences of nitrogen contents in austenitic stainless steel on microstructure, mechanical properties and corrosion resistance were investigated. Results show that the ferrite-austenite phase transformed into single austenite phase after nitriding uptake. The nitrogen contents determined the type of precipitates chromium nitrides, and the contents higher than 2.77 wt. % promoted the formation of CrN, which corresponds well with thermodynamic results. The fine grain size (round 3 μ m) and precipitated chromium nitrides (200~600 nm) lead to a high yield strength of 817-1111MPa, which exceeds conventional stainless steel. The corrosion rate decreased with increasing content up to 1.29 wt. %, then the corrosion rate increased with increasing nitrogen contents, which results from the combined effect of solute nitrogen and nitrides.

1. Introduction

Due to good corrosion resistance and mechanical properties, austenitic stainless steel (ASS) is an indispensable class of alloys and has been widely used from low-end applications in our daily life to very sophisticated ones in industry [1-3]. Conventional ASSs are alloying systems of Fe-Cr-Mn-Ni, which shows the metastable austenite phase and the transformation to martensite improved its strength [4-8]. Although the nickel element is beneficial for improving the corrosion resistance of stainless steel, it also increased the costs of austenitic stainless steel [9] and even caused allergy in the human body when used as biomaterials, such as coronary stent [10, 11]. Therefore, nickel-free high-N austenitic stainless steels of Fe-Cr-Mn-N alloying system and the substitution of Ni by N to reduce the cost of ASSs have attracted much attention in recent decades.

Because of better mechanical properties, higher corrosion resistance and better biocompatibility



[12], nickel-free HNASS attracted extensive attention, which have great potential to be used as structural materials and new coronary stents [13-15]. Nitrogen containing austenitic stainless steels retained high fracture toughness at low temperature, which are successfully applied in the cryogenic industry [16]. As we know, for the HNASS, solute nitrogen is effective to enhance the strength without noticeable decrease of fracture strain [17]. The high nitrogen contents in ASS usually introduce the precipitation of chromium nitrides [18], which precipitated at grain boundary improves the mechanical properties of HNASS [19].

Alloying, pressure metallurgy, powder metallurgy and solution nitriding are the main four methods to improve the nitrogen contents of the HNASS. However, the fabrication of HNASS by pressure metallurgy remains a challenge because it requires expensive casting equipment to ensure pressure around the melting unit [20]. Therefore, powder metallurgy (PM) is thought an effective way to fabricate HNASS with low cost. For austenitic stainless steels (ASSs), solution nitriding could improve the nitrogen contents, but it would also lead to the precipitation of Cr_2N and it depends on the nitrogen contents and annealing temperature [21]. Compared to the hot press sintering, hot isostatic pressing sintering or atmospheric furnaces sintering, spark plasma sintering (SPS) possess many advantages, such as sintering more densification, high heat efficiency, rapid sintering and easy operation [22, 23].

The low strength of f.c.c. ASS impedes its application as structural materials. It is well known that solid solution strengthening, grain boundary strengthening and precipitation hardening are effective ways to enhance the strength of ASS. For pressurized casting HNASS, Simons [24] found that a yield strength of 521-539 MPa and a tensile strength of 945-958 MPa can be obtained, which consists of 10% Cr_2N precipitates. Different from conventional casting method, chemical composition can be more uniform without element segregation in the PM process and an ultrafine grain can also be obtained instead of coarse grain [25], and better mechanical properties can be obtained. Xu et al. [22] fabricated a nickel free HNASS with excellent yield strength and tensile strength of 695 MPa and 847 MPa, respectively.

In this study, a novel approach with a combination of nitriding and powder metallurgy was designed to fabricate a high strength nickel-free HNASS. The influence of nitrogen content on microstructure, mechanical properties and corrosion resistance are studied systematically.

2. Materials and Methods

2.1 Materials fabrication

Spherical nitrogen gas atomized duplex stainless steel powders were adopted, with a chemical composition of 17.75 Cr, 10.84 Mn, 3.40 Mo, 0.36 Ni, 0.05 C, 0.44 N (wt.%), and balance Fe, supplied by Advanced Technology & Materials Co., Ltd, China. Tube furnace was used to perform the nitriding processes under a mixed gas of N_2 : $\text{H}_2=95:5$ (in volume fraction) at 600, 650, 675, 700, 725 and 775 °C for 1 h.

Spark plasma sintering was used to consolidate the nitrided powders at 1000 °C for 480 s in vacuum (<20 Pa) with a the heating rate of 100 °C /min and sintering pressure of 30 MPa. Table 1 shows the corresponding sample codes and details of the experiment.

Table 1 codes and corresponding processing parameters.

Sample code	Detailed processing parameters
S ₀	No nitriding, SPS at 1000 °C
S ₆₀₀	Nitrided at 600 °C for 1 h, SPS at 1000 °C
S ₆₅₀	Nitrided at 650 °C for 1 h, SPS at 1000 °C
S ₆₇₅	Nitrided at 675 °C for 1 h, SPS at 1000 °C
S ₇₀₀	Nitrided at 700 °C for 1 h, SPS at 1000 °C
S ₇₂₅	Nitrided at 725 °C for 1 h, SPS at 1000 °C
S ₇₇₅	Nitrided at 775 °C for 1 h, SPS at 1000 °C

2.2 Microstructural characterization

X-ray diffraction (XRD, D/MAX-2500/PC; Rigaku Corp., Japan) with Cu K α radiation were used to examine the phase constituents. A solution of 5 g FeCl₃ + 50 mL HCl + 100 mL H₂O was used to etching all the samples for microstructure examination by scanning electron microscope (SEM, ZEISS Merlin, Germany). TEM (Tecnai G2 F20 S-TWIN) was used for further phase identification. TEM foils were prepared by argon ion beam thinning. Oxygen and nitrogen gas analyzer (TC600, LECO, USA) was adopted to measure the nitrogen content of all the samples. A NETZSCH STA 449 F3 Differential Scanning Calorimetry (DSC) was used for determining the nitrogen uptake temperature of investigated alloys. The experiments were carried out in a high purity nitrogen gas, at the heating rate of 20 K/min and in the temperature range of 25–1200 °C.

2.3 Mechanical properties

Room temperature tensile stress-strain curve was examined by using a universal testing machine. Tensile tests were performed with a gauge size of 8 mm length, 2 mm width, and 1 mm thickness, which were machined from the sintered cylinder specimen ($\phi 30 \times 12$ mm). Three tensile tests were performed on each alloy at an initial strain rate of $6.25 \times 10^{-4} \text{ s}^{-1}$. Yield stress ($\sigma_{0.2}$) was determined by a 0.2% deviation from the linear elastic stage of the tensile stress-strain curves in all samples. Vickers hardness tester was used to examine the Vickers hardness with a force of 9.8 N (HV1) and a dwell time of 15 s. The hardness values were calculated from averaging 10 measurements. Volume fractions of the precipitations and average grain size of the alloy are determined by counting features in 5 SEM images. In-Situ Nanomechanical Test Instrument (T1750) was used to examine the nanohardness of the investigated alloys. Nanohardness values were calculated from averaging six points for each alloy.

2.4 Immersion test

Immersion test for a total of 240 h in 3.5 wt. % NaCl solution at room temperature was performed to examine the corrosion resistance of each alloy. Cylindrical specimens were machined from the sintered specimens. The surface areas were obtained by examining the height and diameter of each sample. Each sample was ground by 2000 grit abrasive paper and polished by 0.5 μm diamond polishing agent, washed in ethanol by the ultrasound washing machine and weighed (balance accuracy: 0.1 mg) before and after the test. The solution was updated every 48 h to renew the corrosion environment.

3. Results and discussion

3.1 Microstructure investigation

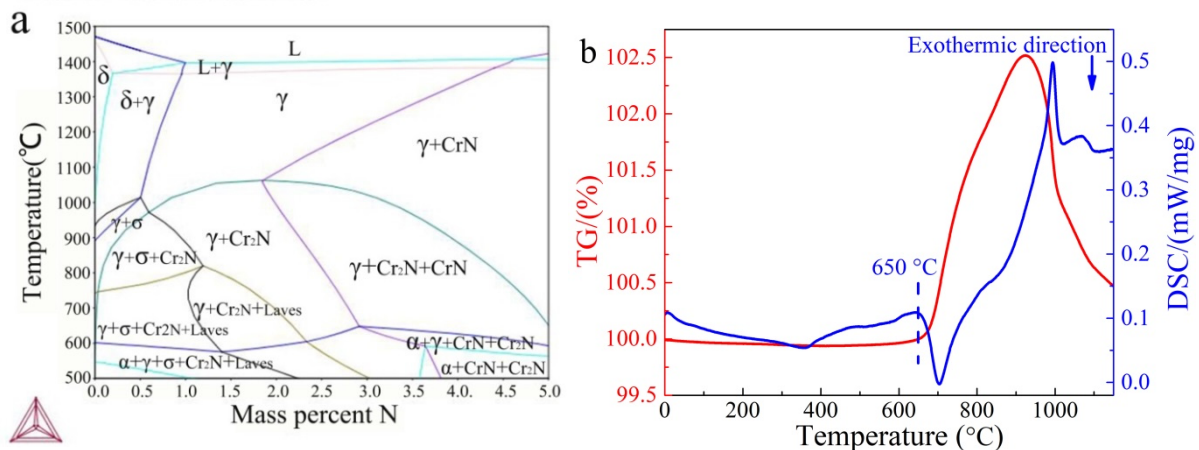
Fig. 1a shows the equilibrium phase diagram of the Fe-17.5Cr-10.8Mn-3.4Mo-xN alloys as a function of various nitrogen contents. Both the temperature and nitrogen content have a decisive role in phase constituent. When temperature ranges between 1000–1200 °C, the phase composition evolution is δ , $\delta+\gamma$, γ , $\gamma+\text{CrN}$, with increasing nitrogen contents; while in the temperature ranging 700–900 °C, the phase composition evolution is $\gamma+\sigma$, $\gamma+\sigma+\text{Cr}_2\text{N}$, $\gamma+\text{Cr}_2\text{N}$, $\gamma+\text{CrN}+\text{Cr}_2\text{N}$ and $\gamma+\text{CrN}$, with the increasing nitrogen contents. The results indicate that low nitrogen contents in investigated alloys promote the formation of Cr_2N , while the high nitrogen contents promote the formation of CrN. At the temperature of 700 °C, the critical nitrogen content to form CrN is around 2.7 wt. %.

Fig. 1b displays the DSC curve of the original powders in nitrogen atmosphere, which provides references for choosing the nitriding temperature. The TG curve shows an increase in weight at a temperature of around 650 °C. Meanwhile, the DSC curve exhibits a single exothermic peak temperature at 710 °C and an endothermic peak temperature of 990 °C, which indicates that the ferrite phase starts transforming into austenite phase at the temperature of 650 °C. According to the equilibrium phase diagram in Fig. 1a, the ferrite phase starts transforming into austenite phase at the temperature of 600 °C. The differences in experimental and thermodynamic temperature may result from the rapid heating rate of 20 K/min. Additionally, the nitrogen uptake and manganese sublimation

[26] also would affect the TG and DSC curves.

XRD experiments were conducted to identify the phase constituent of both the nitrated powders and SPS-ed bulk alloys. As seen in Fig. 1c, the original powders (X15) consist of austenite (FCC) and ferrite (BCC). After nitriding at 700 °C for 1h, diffraction peaks of Cr₂N could be detected. And the intensity of diffraction peaks for austenite increased and those for ferrite decreased, indicating that the nitrogen uptake promotes the ferrite-to-austenite transformation. Gavriljuk et al. [27, 28] found that carbon+nitrogen increased the concentration of conduction electrons and thus increases the thermodynamic stability of the γ -phase. More strikingly, for powders nitrated at 800 °C for 1h, diffraction peaks corresponding to ferrite were not observed, suggesting that the ferrite transforms into austenite. As already known, the increasing nitrogen contents in solid solution expanded austenite phase zone [20]. Additionally, the diffraction peaks corresponding to Cr₂N and CrN also were observed. Only diffraction peaks of austenite and CrN were detected since the nitriding temperature increases to 900 °C. Valencia-Alvarado et al. reported nitriding of bulk AISI 304 stainless steel in a 85% H₂/15% N₂ mixture and expanded γ_N phase occurred, and also found that the nitrated depth is a function of the sample temperature [29].

The XRD patterns of bulk HNASSs after spark plasma sintering were shown in Fig. 1d. Apparently, the matrix of all the alloys with various nitriding temperatures, including the S₀ alloy, is austenite phase. The nitriding temperatures have significant effects on the precipitation of CrN and Cr₂N. Only diffraction peaks of austenite can be detected in S₀ alloy and no other diffraction peaks can be observed. While in the S₆₅₀ alloy, diffraction peaks of Cr₂N phase is obvious. As the nitriding temperature rises from 650 to 700 °C, the intensity of the diffraction peak of Cr₂N phase becomes stronger. Above the nitriding temperature of 725 °C, the diffraction peaks of CrN could be detected. However, only CrN and austenitic diffraction peaks were detected in S₇₇₅ alloy. This phenomenon results from the change of nitriding temperature and corresponding N content of the alloys. The type of precipitation, to be Cr₂N, Cr₂N + CrN or CrN, was determined by the nitrogen content of the alloy. All the results suggest that the nitrogen contents in alloys increased with increasing temperature and determined the precipitated chromium nitrides type. The experimental results are consistent with thermodynamic results.



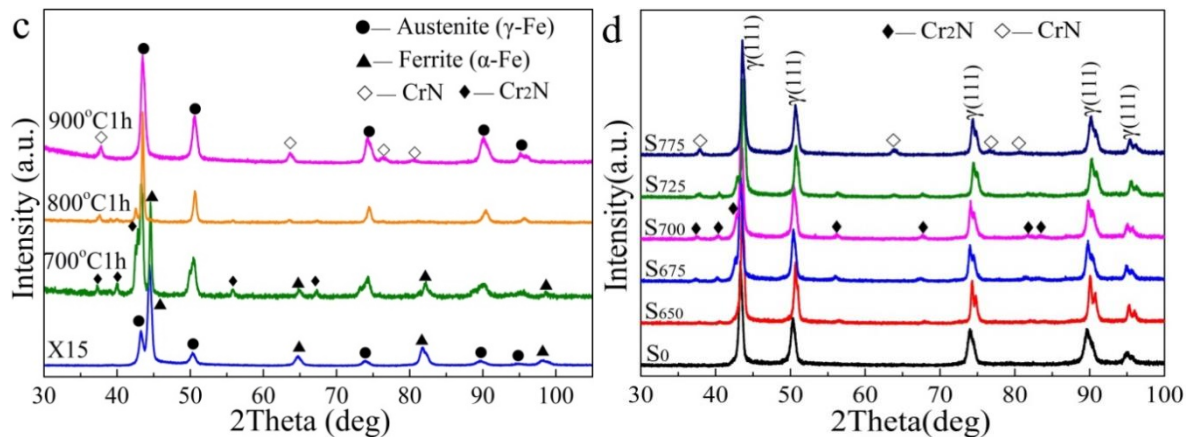


Fig. 1. (a) Thermodynamic calculation of equilibrium phase fractions for Fe-17.5Cr-10.8Mn-3.4Mo-xN; (b) DSC pattern of the original powders under N₂ atmosphere at the heating rate of 20 K/min; XRD patterns of (c) the nitrided powder and (d) the nitrided and SPS-ed HNASSs with various nitriding temperatures.

Figs. 2 show the microstructural evolution of the SPS-ed HNASSs with various nitriding temperatures and various nitrogen contents, which was recorded by secondary electron (SE) image. Few precipitated nitrides at the grain boundary can be seen in the alloy S₀, but it is not detected by XRD, as shown in Fig. 2a. As the nitriding temperature rises, both the size and amounts of the precipitation increase, as shown in Fig. 2b and 2d. Since the ASS would be consolidated at a high temperature of 1000 °C, the precipitated chromium nitrides are thought to be helpful in pinning the grain boundary and thus impede the coarsening of grains. According to its microstructure shown in Figs. 2, the average grain size of the S₀, S₆₅₀, S₇₀₀ and S₇₇₅ alloy are identified to be around 7.1, 2.4, 1.7 and 1.6 μm, respectively.

As already known, the average size and volume fraction of the precipitated particles significantly influence the microstructure of alloys. Yong [30] indicated that the critical grain size of the alloy is closely related to the volume fraction and the average size of precipitates, which can be expressed as follow:

$$D_c = \frac{\pi d}{6f} \left(\frac{3}{2} - \frac{2}{Z} \right) \quad (1)$$

where D_c is the critical grain size, d is the average size and f is the volume fraction of chromium nitrides precipitates in the alloys, and Z is a constant and 1.7 was chosen most frequently [31]. For the chromium nitrides, its effects on coarsening of austenite grain size also could be applied.

According to the SE images, the volume fraction of chromium nitrides in alloys S₀, S₆₅₀, S₇₀₀ and S₇₇₅ reached 3.09 %, 7.86 %, 10.43 %, 11.83 %, respectively. The average size of precipitated particles in alloy S₀, S₆₅₀, S₇₀₀ and S₇₇₅ are 0.65, 0.33, 0.38 and 0.41 μm respectively. Therefore, the critical grain size for alloys S₀, S₆₅₀, S₇₀₀ and S₇₇₅ should be 3.56, 0.71, 0.62 and 0.59 μm. The experimentally determined grain size in Figure 2(a) seems to be larger than the calculated critical grain size by the above equation. This could be ascribed to two aspects: firstly, the interaction between the Cr₂N phase and CrN phase was not taken into account; secondly, the actual size of nitrides fluctuated in the range of 0 to 1 μm, rather than being an average value. All the results indicate that the nano-sized particles have a stronger effect on grain size coarsen during the sintering process.

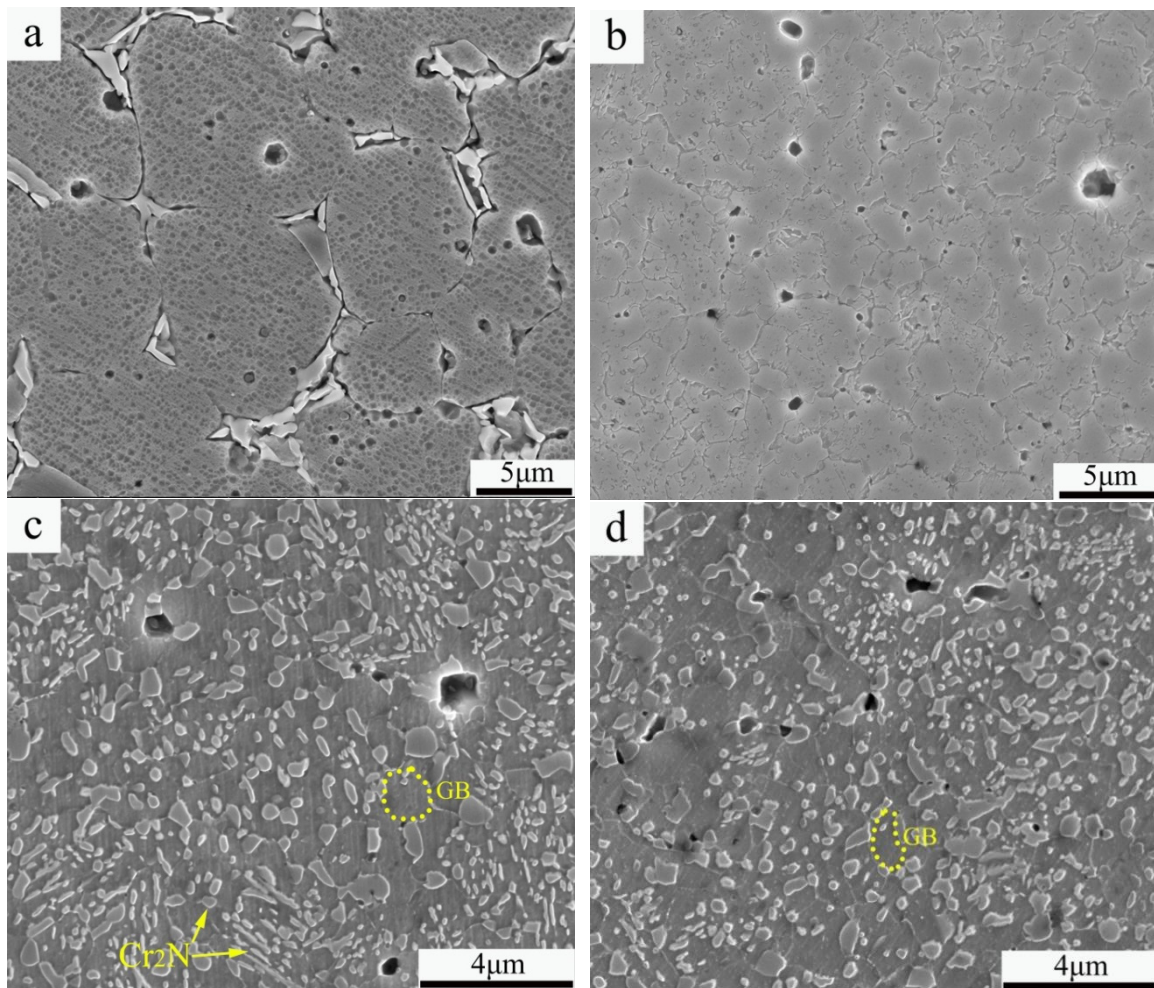


Fig. 2. SE micrographs of austenitic stainless steel nitrided at different temperatures: (a) S_0 ; (b) S_{650} ; (c) S_{700} ; (d) S_{775} .

To further identify the precipitated particles, the microstructure of the specimens S_{775} by TEM test is shown in Figs. 3. The average chemical compositions of precipitated particles in Fig. 3a and 3c measured by EDS are $Cr_{67.47}Fe_{0.89}Mn_{1.03}N_{30.15}$ and $Cr_{51.36}Fe_{0.6}Mn_{0.84}N_{46.68}$ (at. %), respectively. The selected area diffraction pattern (SADP) inset in Fig. 3a and 3c both demonstrates a face-centered cubic (f.c.c.) structure. The precipitated particles are identified to be chromium-rich CrN compounds based on the EDS and SADP results, because the Cr_2N possess a hexagonal close-packed (HCP) structure. And the nitrogen contents in S_{775} alloy reaches 2.62 wt. %. According to the XRD results, no diffraction peaks of Cr_2N were detected, and the TEM further confirmed that merely CrN compounds were found in the alloy with 2.62 wt. % nitrogen contents (alloy S_{775}).

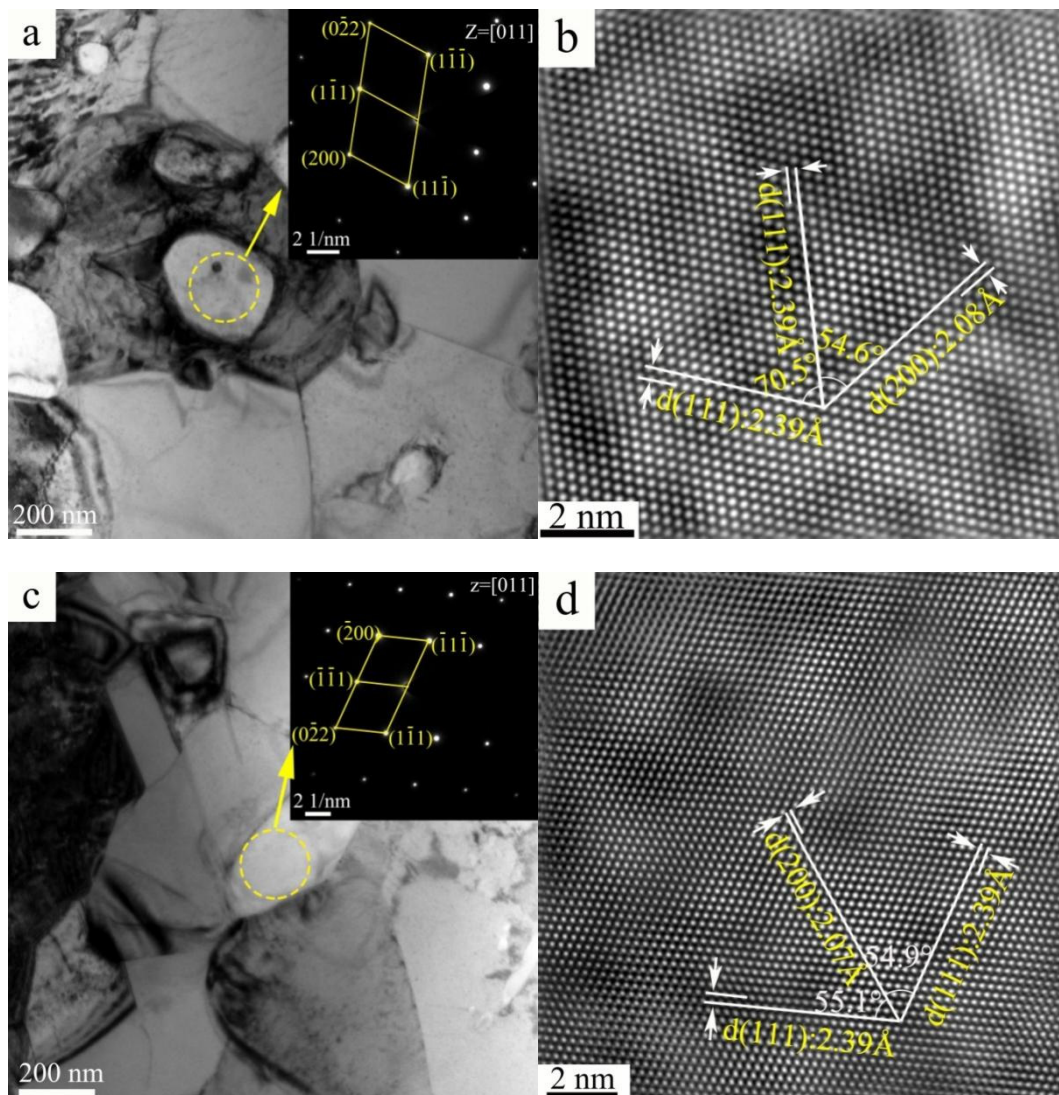


Fig. 3. The microstructure of the S775 alloy: (a) Bright-field image of grain boundary containing equiaxed nitrides; (b) High-resolution TEM image of selected area in (a); (c) Bright-field image of grain boundary containing non-equiaxed nitrides; (d) High-resolution TEM image of selected area in (c).

3.2 Thermodynamic analysis

The mole fraction of Cr_2N and CrN as a function of nitrogen contents were shown in Fig. 4a and 4b, with a temperature ranging 600~1200 °C, which was obtained based on the CALPHAD (Calculation of Phase Diagrams). For alloys nitrated at 600 °C, the nitrogen content was identified to be 0.75 wt. %, as shown in Table 2. And the corresponding thermodynamic results show the content of Cr_2N is around 7.5 % in mole fraction. When nitrating temperature increased to 700 °C, the nitrogen content was increased to striking 1.96 wt. %, and the microstructure with around 20 % Cr_2N precipitates would be obtained. With regard to the CrN precipitates, at the temperature below 800 °C, the nitrogen contents of at least 2.55 wt. % would promote the formation of CrN precipitates. All the results further confirm that the nitrogen contents determined the type of chromium nitrides.

Nitrating process is very complicated, which is usually accompanied by precipitation and there were two types of chromium nitrides. And the precipitation of chromium nitrides can be predicted and analyzed in thermodynamic, including the type and volume fraction. When the nitrogen contents exceed the threshold contents, the diffused nitrogen starts to nucleate and precipitate. Consider the

action:



The difference in Gibbs free energy of precipitated Cr₂N and CrN could be described as Eq. 2 and 3, respectively, where G_i^0 is the free energy of component i in its standard state, R is the ideal gas constant, T is absolute temperature, and the difference in free energy for the nitrides precipitation reaction:

$$\frac{1}{2}\Delta^0 G_{\text{Cr}_2\text{N}} = \frac{1}{2}G_{\text{Cr}_2\text{N}}^0 - G_{\text{Cr}}^0 - \frac{1}{2}G_{\text{N}}^0 = RT\log(a_{\text{Cr}}^\gamma a_{\text{N}}^{\gamma 1/2}) \tag{4}$$

based on the assumption that the activity of the pure Cr₂N compound is 1. The activity of each component is related to the mole fraction, Xi, in solution in austenite by the relation:

$$a_i^\gamma = \Gamma_i^\gamma \times X_i^\gamma \tag{5}$$

where Γ_i is the activity coefficient of component i. Substituting and rearranging yields:

$$X_{\text{Cr}} X_{\text{N}}^{1/2} = (\Gamma_{\text{Cr}}^\gamma)^{-1} \times (\Gamma_{\text{N}}^\gamma)^{-1/2} \times \exp\left(\frac{\Delta^0 G_{\text{Cr}_2\text{N}}}{2RT}\right) \tag{6}$$

$$X_{\text{Cr}} X_{\text{N}} = (\Gamma_{\text{Cr}}^\gamma)^{-1} \times (\Gamma_{\text{N}}^\gamma)^{-1} \times \exp\left(\frac{\Delta^0 G_{\text{CrN}}}{2RT}\right) \tag{7}$$

Eqs. 6 and 7 represent the Solubility products of Cr₂N and CrN in austenite at equilibrium state, which aids in alloy design of secondary hardening steels used in high nitrogen stainless steels applications [32]. For the investigated HNASS, the difference in Gibbs free energy of Cr₂N ($\Delta^0 G_{\text{Cr}_2\text{N}}$) and CrN ($\Delta^0 G_{\text{CrN}}$) could be seen in Fig. 5a and 5b. From Fig. 5a, it can be seen that high nitrogen contents in HNASS contributed to lower value of $\Delta^0 G_{\text{Cr}_2\text{N}}$. Based on the solubility products of Cr₂N, the lower value of $\Delta^0 G_{\text{Cr}_2\text{N}}$ would result in less amount of dissolved chromium and nitrogen contents, indicating more Cr₂N precipitated with increasing nitrogen contents in thermodynamics.

Additionally, the CALPHAD results in Fig. 1a indicates that the critical nitrogen contents for Cr₂N and CrN precipitation are 2.7 wt. %, which was also in good agreement with SEM and XRD results. In the present study, the nitriding temperature of around 750 °C was chosen and the nitrogen exceeds the solid solubility of nitrogen in austenite phase. The difference in Gibbs free energy for Cr₂N precipitation is around -24 KJ/mol, while the precipitation of CrN contributes to the decrease of around -14 KJ/mol. Therefore, when the nitrogen contents are below 2.7 wt. %, precipitation of Cr₂N resulted in a lower change in Gibbs energy; While the nitrogen contents exceed the critical content of 2.7 wt. %, precipitation of CrN resulted in a lower change in Gibbs energy.

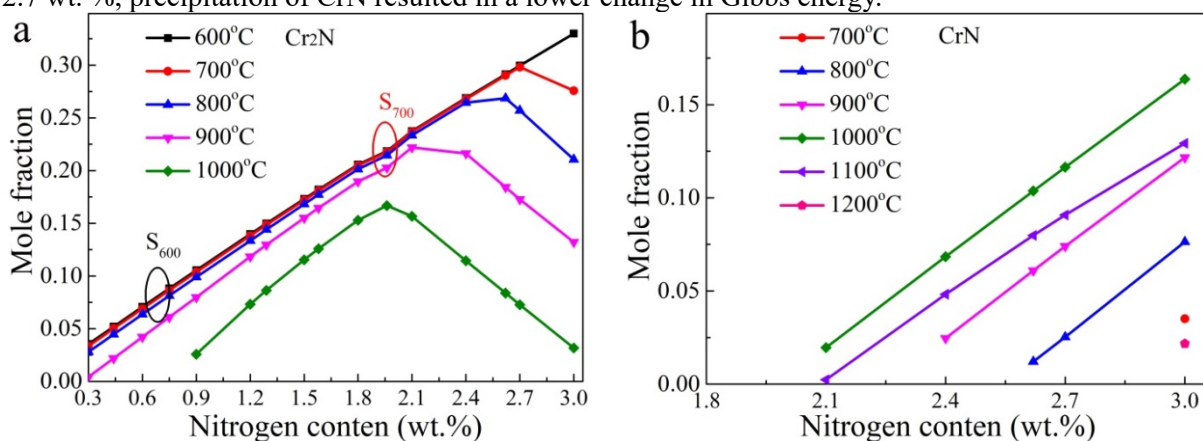


Fig. 4. Mole fraction of precipitated (a) Cr₂N and (b) CrN as a function of the nitrogen contents at various temperatures.

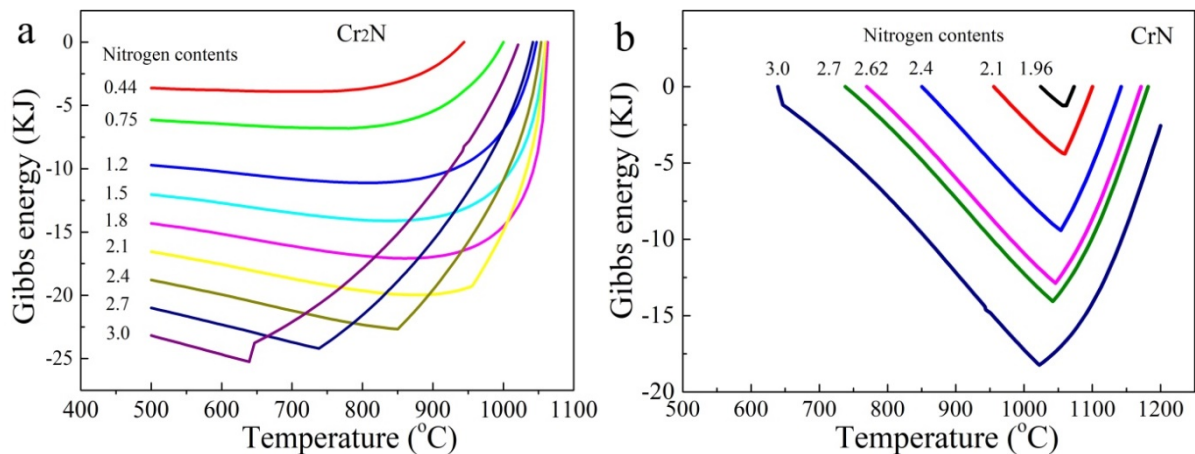


Fig. 5. Calculated change in Gibbs free energy by ThermoCalc as a function of various temperature and nitrogen contents: (a) Cr_2N and (b) CrN .

3.3 Mechanical properties

Both the nitriding temperature and nitrogen content have a significant effect on the hardness and tensile strength of nickel-free high-N austenitic stainless steel. The Vickers hardness and in situ nano-hardness varying with nitrogen content of the alloys are shown in Table 2. The nitrogen content range between 0.75~2.62 wt. % after nitriding at 600~775 °C indicating that the nitrogen content can be adjusted by controlling the nitriding temperature. The in situ nano-hardness of austenite increased with increasing nitrogen contents, which can be attributed to the solute nitrogen strengthening and grain boundary strengthening.

Table 2 In situ nano-hardness and Vickers hardness (HV) varying with nitrogen content of the PM SPS-ed high N austenitic steel.

Sample codes	S ₀	S ₆₀₀	S ₆₅₀	S ₆₇₅	S ₇₀₀	S ₇₂₅	S ₇₇₅
N content (wt. %)	0.44	0.75	1.29	1.58	1.96	2.14	2.62
Hardness (HV)	436 ± 4.0	445 ± 3.4	454 ± 4	477 ± 5	478 ± 4	496 ± 4	504 ± 4
Hardness(GPa)	5.5 ± 0.2	5.6 ± 0.2	7.0 ± 0.2	7.4 ± 0.2	7.5 ± 0.3	7.9 ± 0.3	8.1 ± 0.2

Fig. 6a presents tensile stress-strain curves at room temperature for the as-prepared HNASSs with various nitriding temperatures. Fig. 6b shows the variation of yield strength, ultimate tensile strength and strain to fracture of the as-prepared alloys. When the temperature of solution nitriding improved to 650 °C, the yield strength and ultimate tensile strength rises strongly to 1067 MPa and 1264 MPa respectively, while the fracture strain declined to a low value of 11.0 %. Compared to alloy S₆₀₀ nitrided at 600 °C, the yield strength of the alloy S₆₅₀ increased by 55% and the tensile strength increased by 23%, indicating that the solid solution strengthening from nitrogen was pronounced and it increased the yield strength more than the tensile strength. This significantly increase is mainly attributed to the increased nitrogen content rise from 0.75 to 1.29 wt. %. This increase in nitrogen content results in both an increase of nitrogen contents in solid solution and amounts of nano-sized precipitated nitrides. Both solid solution strengthening and precipitation hardening contribute to the increase of mechanical properties.

The nitrogen content is reported to have a profound effect on the yield strength, ultimate tensile strength and strain to fracture of the high nitrogen austenitic stainless steel [33, 34]. While the nitriding temperature is up to 675 °C and the corresponding nitrogen content exceeds 1.58 wt.%, both the tensile strength and yield strength began to decline. Similar results were also observed earlier [19]. The fracture strain of nickel-free HNASS decreased with increasing nitrogen content. This obvious drop in fracture strain is caused by such a high concentration of nitrides, as shown in Figs. 2. It means that the best nitriding temperature is around 600 to 650 °C, and the best combination of tensile strength and strain to fracture can be obtained with a solution nitriding time of 1 h. The mechanical

properties of nickel-free HNASSs fabricated in this study are much higher than other HNASSs reported in the published literature [19, 35]. All the results suggest that this PM SPS-ed HNASS has a good combination of strength and toughness.

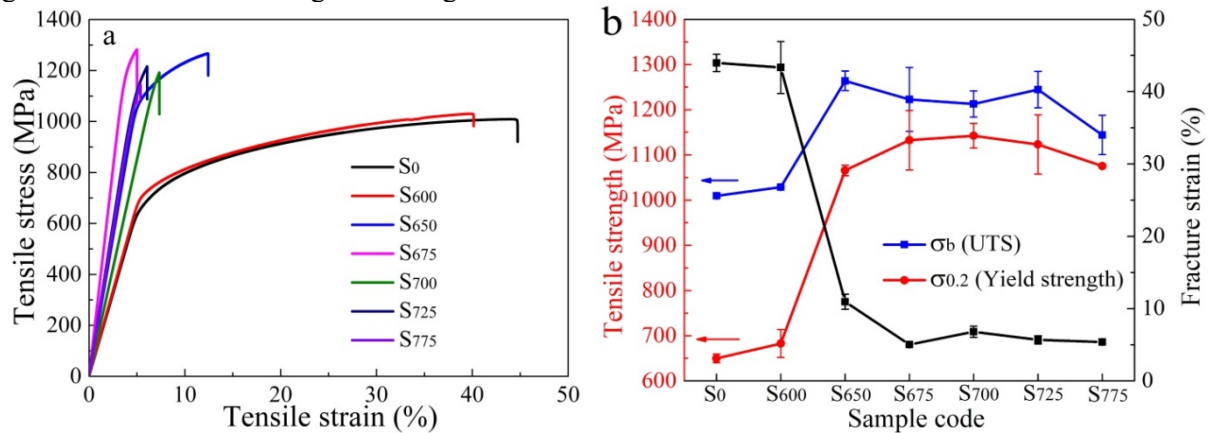
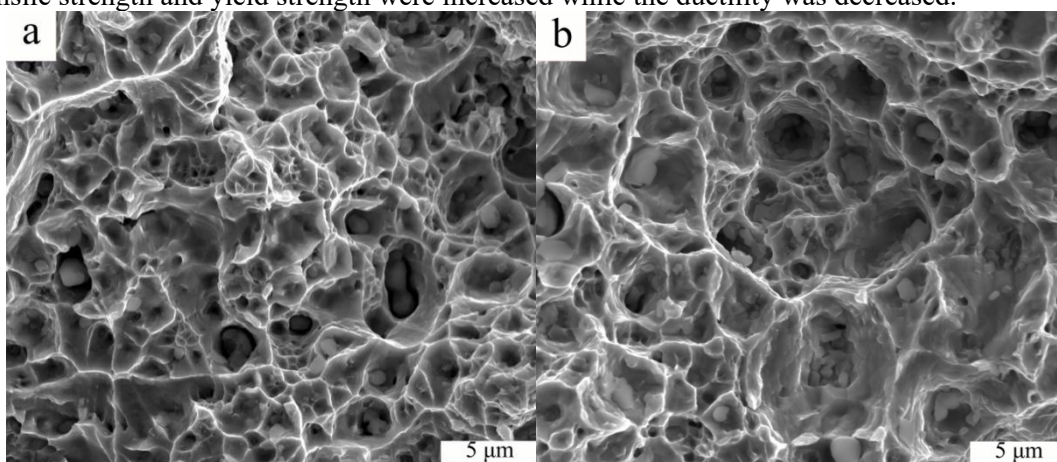


Fig. 6. (a) Engineering stress-strain curves of tensile tests of the as-prepared HNASSs and (b) yield strength, tensile strength and strain to fracture of the as-prepared HNASS with different nitriding temperature.

The fracture surfaces of the as-prepared high N austenitic stainless steel after tensile tests are illustrated in Fig. 7 of the S₀, S₆₀₀, S₆₅₀ and S₆₇₅ alloy. All four conditions show a ductile fracture mode with striking dimples and dimples of varying size can be observed, which results from the growth of neighboring microvoids before the materials rupturing. Microvoids could originate from various phase interface and inner free surfaces between matrix and precipitates. The inner free surfaces develop into globular voids and even emerge to form an increase of fracture with increasing stress. [36]. As is shown in Figs. 7a and 7b, some very fine dimples which were formed during emerge many larger spherical voids surround some of the coarse dimples. With increasing nitriding temperature and thus nitrogen content, one can see that the dimple size becomes smaller, but the amount of dimples increases. The excellent ductility of S₀ and S₆₀₀ sample is ascribed to the FCC structure of austenite matrix and no nitrides precipitates. Solid solution hardening of solute nitrogen and precipitation strengthening of chromium nitrides caused more brittle fracture in alloy S₆₇₅, S₇₀₀, S₇₂₅, S₇₇₅, thus both the tensile strength and yield strength were increased while the ductility was decreased.



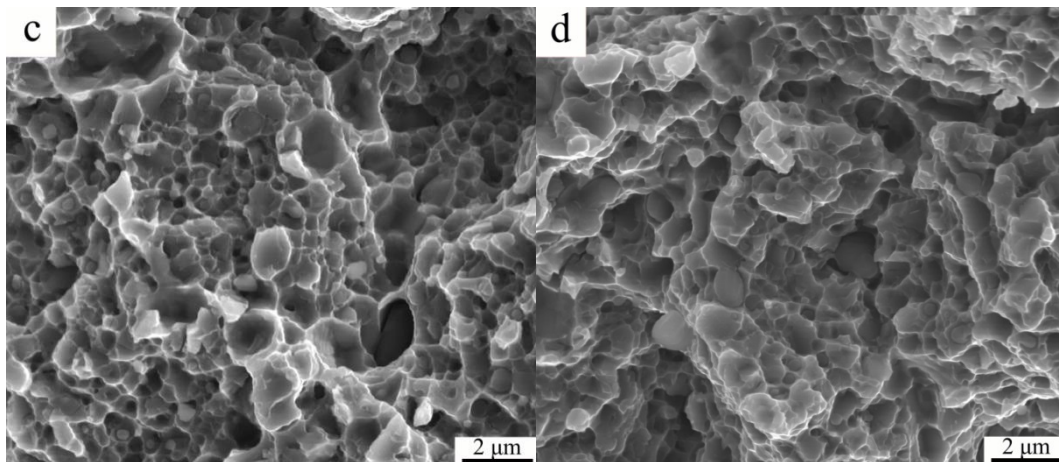


Fig. 7. Fracture surface of as-prepared HNASS with various nitriding temperature of (a) S₀; (b) S₆₀₀; (c) S₆₅₀; (d) S₆₇₅.

3.4 Corrosion resistance

To explore the effects of nitrogen contents on corrosion resistance of HNASS, the immersion corrosion test in 3.5 wt. % NaCl solution was conducted. Fig. 8a shows the weight loss varying with immersion time and nitrogen contents. It can be observed that the weight loss increased monotonously with the immersion time. After being immersed for 48-240 h, S₆₅₀ alloy exhibits the minimum weight loss and S₇₇₅ alloy shows the maximum weight loss, indicating that S₆₅₀ alloy has the strongest corrosion resistance and S₇₇₅ alloy has poorest corrosion resistance. The influences of nitrogen contents on corrosion resistance of ASS are very complex: (1) the solute nitrogen improves the corrosion resistance of ASS [37-39]; (2) while the precipitated chromium nitrides deteriorate the corrosion resistance of ASS [40, 41].

Fig. 8b shows the variation of the corrosion rate, as a function of nitriding temperature and N content for the HNASSs. With increasing nitriding temperature, the corrosion rate declined to the lowest value of 0.004 mg/cm²·h (650 °C) at first, and then increased to the highest value of 0.008 mg/cm²·h (775 °C), suggesting that the nitrogen contents of 1.29 wt.% is a critical content to obtain optimum corrosion resistance for investigated HNASS. The corrosion rate of HNASS in this study is similar to those of conventional Fe-Ni-Cr ASS [42, 43]. The nitriding temperature and nitrogen contents have a significant influence on the corrosion rate of HNASSs. The relationship between the pitting resistance equivalent and chemical composition could be expressed as an empirical formula [37]: PRE = Cr + 3.3Mo + 16N. Accordingly, higher nitriding temperature contributes to higher nitrogen contents in solid solution, which thus resulted in better corrosion resistance [35]. The increase in resistance to the uniform corrosion in this solution for the S₆₀₀ and S₆₅₀ alloy is mainly ascribed to the increase in solute nitrogen and absence of large quantitative of nitrides precipitates. As the nitrogen content increase to 1.58~2.62 wt. % in S₆₇₅, S₇₀₀, S₇₂₅ and S₇₇₅ alloys, large amounts of nitrides precipitated (as shown in Figs. 2c and 2d) result in the increase of Cr depletion area and phase boundary, thus accelerating the corrosion rate and finally deteriorate the corrosion resistance. All the results mean that the as-fabricated HNASSs feature both high mechanical property and excellent corrosion resistance, which is important to the application of austenitic stainless steel.

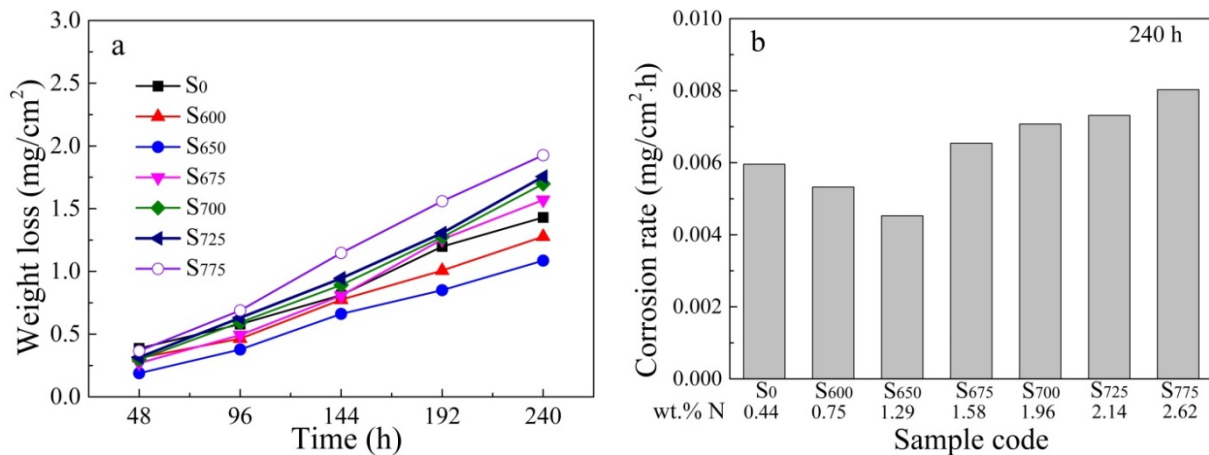


Fig. 8. (a) Weight loss varies with nitrogen contents and corrosion time; (b) Variation of the corrosion rate as a function of nitriding temperature and nitrogen content.

4. Conclusions

A nickel-free high nitrogen austenitic stainless steel was prepared by a innovation method consisting of solution nitriding and powder metallurgy. The influences of nitrogen contents in austenitic stainless steel on microstructure, mechanical properties and corrosion resistance were investigated in detail, and the following conclusions were reached:

1. Nitriding obviously improves nitrogen contents in high-N austenitic stainless steel and contributes the ferrite-austenite phase transforming to austenite phase. Both experiments and thermodynamic analysis confirmed that nitrogen contents higher than 2.77 wt. % promotes the formation of CrN and lower than the value favors the formation of Cr₂N. The nano-sized nitrides impede coarsen of austenite grain size during the SPS sintering.

2. The fine grain size (round 3μm) and chromium nitrides precipitates (200~600nm) resulted in a high yield strength of 817-1111 MPa, which exceeds conventional austenitic stainless steel. The increase in nitrogen contents in nickel free high nitrogen austenitic stainless steel resulted in improvement of both the tensile strength and yield strength, but a decline in strain to fracture. The best nitriding temperature is around 600-650 °C to obtain the best combination of tensile strength and fracture strain while the solution nitriding time of 1 h.

3. The corrosion rate decreased with increasing nitrogen content up to 1.29 wt. %, but the corrosion rate increased with increasing nitrogen contents, which results from the combined effect of solute nitrogen and nitrides.

Acknowledgments

The authors gratefully acknowledge financial support from the National Natural Science Fund of China (51675124);Guangdong Science and Technology Project (2017B090907015); and Major Project of Department of Education of Guangdong Province (2017GCZX003). The authors also acknowledge Xing Wei for his support for the ThermoCalc calculations at the Wuhan Branch of Baosteel Central Research Institute, R & D Center of Wuhan Iron & Steel Co., Ltd.

References

- [1] K.H. Lo, C.H. Shek, J.K.L. Lai, Recent developments in stainless steels, *Mater. Sci. Eng. R*, 65 (2009) 39-104.
- [2] S. Wang, J. Li, Y. Cao, B. Gao, Q. Mao, Y. Li, Thermal stability and tensile property of 316L stainless steel with heterogeneous lamella structure, *Vacuum*, 152 (2018) 261-264.
- [3] J. Li, B. Gao, Z. Huang, H. Zhou, Q. Mao, Y. Li, Design for strength-ductility synergy of 316L stainless steel with heterogeneous lamella structure through medium cold rolling and annealing, *Vacuum*, 157 (2018) 128-135.

- [4] S. Gao, Y. Bai, R.X. Zheng, Y.Z. Tian, W.Q. Mao, A. Shibata, N. Tsuji, Mechanism of huge Lüders-type deformation in ultrafine grained austenitic stainless steel, *Scr. Mater.*, 159 (2019) 28-32.
- [5] Y. Xiong, Y. Yue, Y. Lu, T.T. He, M.X. Fan, F.Z. Ren, W. Cao, Cryorolling impacts on microstructure and mechanical properties of AISI 316 LN austenitic stainless steel, *Mater. Sci. Eng. A*, 709 (2018) 270-276.
- [6] Y.C. Zhang, M.C. Li, H.Y. Bi, J.Q. Gu, D.X. Chen, E. Chang, W. Zhang, Martensite transformation behavior and mechanical properties of cold-rolled metastable Cr-Mn-Ni-N austenitic stainless steels, *Mater. Sci. Eng. A*, 724 (2018) 411-420.
- [7] M.C. Somani, P. Juntunen, L.P. Karjalainen, R.D.K. Misra, A. Kyröläinen, Enhanced Mechanical Properties through Reversion in Metastable Austenitic Stainless Steels, *Metall. Mater. Trans. A*, 40 (2009) 729-744.
- [8] M. Naghizadeh, H. Mirzadeh, Modeling the kinetics of deformation-induced martensitic transformation in AISI 316 metastable austenitic stainless steel, *Vacuum*, 157 (2018) 243-248.
- [9] M.O. Speidel, Nitrogen Containing Austenitic Stainless Steels, *Materialwiss. Werkstofftech.*, 37 (2006) 875-880.
- [10] J. Li, Y.X. Yang, Y.B. Ren, J.H. Dong, K. Yang, Effect of cold deformation on corrosion fatigue behavior of nickel-free high nitrogen austenitic stainless steel for coronary stent application, *J. Mater. Sci. Technol.*, 34 (2017) 660-665.
- [11] L. Hu, T.W. Ngai, H.L. Peng, L.J. Li, F. Zhou, Z.W. Peng, Microstructure and properties of porous high-N Ni-free austenitic stainless steel fabricated by powder metallurgical route, *Materials*, 11 (2018) 1058.
- [12] T. Ma, P. Wan, Y. Cui, G. Zhang, J. Li, J. Liu, Y. Ren, K. Yang, L. Lu, Cytocompatibility of High Nitrogen Nickel-Free Stainless Steel for Orthopedic Implants, *J. Mater. Sci. Technol.*, 28 (2012) 647-653.
- [13] Y. Ren, H. Zhao, W. Liu, K. Yang, Effect of cold deformation on pitting corrosion of 00Cr18Mn15Mo2N0.86 stainless steel for coronary stent application, *Mater. Sci. Eng. C*, 60 (2016) 293-297.
- [14] P. Wan, Y. Ren, B. Zhang, K. Yang, Analysis of Magnetism in High Nitrogen Austenitic Stainless Steel and Its Elimination by High Temperature Gas Nitriding, *J. Mater. Sci. Technol.*, 27 (2011) 1139-1142.
- [15] W. Zhu, H. Zhang, C. Guo, Y. Liu, X. Ran, Wetting and brazing characteristic of high nitrogen austenitic stainless steel and 316L austenitic stainless steel by Ag-Cu filler, *Vacuum*, 166 (2019) 97-106.
- [16] V.G. Gavriljuk, Nitrogen in Iron and Steel, *ISIJ Int.*, 36 (1996) 738-745.
- [17] T.H. Lee, S.J. Kim, S. Takaki, Time-Temperature-Precipitation Characteristics of High-Nitrogen Austenitic Fe-18Cr-18Mn-2Mo-0.9N Steel, *Metall. Mater. Trans. A*, 37 (2006) 3445-3454.
- [18] T.-H. Lee, H.-Y. Ha, S.-J. Kim, Precipitation of Second Phases in High-Interstitial-Alloyed Austenitic Steel, *Metall. Mater. Trans. A*, 42 (2011) 3543-3548.
- [19] V.G. Gavriljuk, H. Berns, C. Escher, N.I. Glavatskaya, A. Sozinov, Y.N. Petrov, Grain boundary strengthening in austenitic nitrogen steels, *Mater. Sci. Eng. A*, 271 (1999) 14-21.
- [20] V.G. Gavriljuk, H. Berns, *High Nitrogen Steels: Structure, Properties, Manufacture, Applications*, Springer-Verlag Berlin Heidelberg New York, 1999.
- [21] A. Martinavičius, G. Abrasonis, A.C. Scheinost, R. Danoix, F. Danoix, J.C. Stinville, G. Talut, C. Templier, O. Liedke, S. Gemming, W. Möller, Nitrogen interstitial diffusion induced decomposition in AISI 304L austenitic stainless steel, *Acta Mater.*, 60 (2012) 4065-4076.
- [22] Z.W. Xu, C.C. Jia, C.J. Kuang, K. Chu, X.H. Qu, Spark plasma sintering of nitrogen-containing nickel-free stainless steel powders and effect of sintering temperature, *J. Alloys Compd.*, 484 (2009) 924-928.
- [23] H.W. Ni, H. He, G.Q. Li, J. Liu, Preparation of nanocrystalline 430L stainless steel by HEBM and

- SPS, *J. Iron Steel Res. Int.*, 15 (2008) 73-76.
- [24] J.W. Simmons, Influence of nitride (Cr₂N) precipitation on the plastic flow behavior of HIGH-NITROGEN austenitic stainless steel, *Scr. Metall. Mater.*, 32 (1995) 265-270.
- [25] H.L. Peng, L. Hu, L.J. Li, L.Y. Zhang, X.L. Zhang, Evolution of the microstructure and mechanical properties of powder metallurgical high-speed steel S390 after heat treatment, *J. Alloys Compd.*, 740 (2018) 766-773.
- [26] K. Zumsande, A. Weddeling, E. Hryha, S. Huth, L. Nyborg, S. Weber, N. Krasokha, W. Theisen, Characterization of the surface of Fe-19Mn-18Cr-C-N during heat treatment in a high vacuum- An XPS study, *Mater. Charact.*, 71 (2012) 66-76.
- [27] V.G. Gavriljuk, B.D. Shanina, H. Berns, Ab initio development of a high-strength corrosion-resistant austenitic steel, *Acta Mater.*, 56 (2008) 5071-5082.
- [28] V.G. Gavriljuk, B.D. Shanina, H. Berns, A physical concept for alloying steels with carbon+nitrogen, *Mater. Sci. Eng. A*, 481-482 (2008) 707-712.
- [29] R. Valencia-Alvarado, A. de la Piedad-Beneitez, J. de la Rosa-Vázquez, R. López-Callejas, S.R. Barocio, O.G. Godoy-Cabrera, A. Mercado-Cabrera, R. Peña-Eguiluz, A.E. Muñoz-Castro, Nitriding of AISI 304 stainless steel in a 85% H₂/15% N₂ mixture with an inductively coupled plasma source, *Vacuum*, 82 (2008) 1360-1363.
- [30] Q.L. Yong, *Secondary Phases in Steels*, Metallurgy Industry Press, Beijing, 2006.
- [31] H.L. Peng, L. HU, X.L. Zhang, X. Wei, L.J. Li, J.Y. Zhou, Microstructural evolution, behavior of precipitates, and mechanical properties of powder metallurgical high-speed steel S390 during tempering, *Metall. Mater. Trans. A*, 50 (2019) 874–883.
- [32] E.J. Pavlina, J.G. Speer, C.J.V. Tyne, Equilibrium solubility products of molybdenum carbide and tungsten carbide in iron, *Scr. Mater.*, 66 (2012) 243-246.
- [33] P. Milliner, C. Solenthaler, P. Uggowitz, M.O. Speidel, On the effect of nitrogen on the dislocation structure of austenitic stainless steel, *Mater. Sci. Eng. A*, 164 (1993) 164-169.
- [34] M.O. Speidel, New nitrogen-bearing austenitic stainless steel, *Met. Sci. Heat Treat.*, 47 (2005) 9-13.
- [35] P.J. Uggowitz, R. Magdowski, M.O. Speidel, Nickel free high nitrogen austenitic steels, *ISIJ Int.*, 36 (1996) 901-908.
- [36] I.d. Diego-Calderón, I. Sabirov, J.M. Molina-Aldareguia, C. Föjer, R. Thiessen, R.H. Petrov, Microstructural design in quenched and partitioned (Q&P) steels to improve their fracture properties, *Mater. Sci. Eng. A*, 657 (2016) 136-146.
- [37] J.O. Nilsson, A. Wilson, Influence of isothermal phase transformations on toughness and pitting corrosion of super duplex stainless steel SAF 2507, *Mater. Sci. Technol.*, 9 (1993) 545-554.
- [38] Y.S. Yoon, H.Y. Ha, T.H. Lee, S. Kim, Comparative study of stress corrosion cracking susceptibility of Fe₁₈Cr₁₀Mn- and Fe₁₈Cr₁₀Mn₁Ni-based high nitrogen stainless steels, *Corros. Sci.*, 88 (2014) 337-348.
- [39] J.W. Simmons, Mechanical properties of isothermally aged high-nitrogen stainless steel, *Metall. Mater. Trans. A*, 26A (1995) 2085-2101.
- [40] R.D. Knutsen, C.I. Lang, J.A. Basson, Discontinuous cellular precipitation in a Cr–Mn–N steel with niobium and vanadium additions, *Acta Mater.*, 52 (2004) 2407-2417.
- [41] R.A. Perren, T. Suter, C. Solenthaler, G. Gullo, P.J. Uggowitz, H. Bohni, M.O. Speidel, Corrosion resistance of super duplex stainless steels in chloride ion containing environments: investigations by means of a new microelectrochemical method II. Influence of precipitates, *Corros. Sci.*, 43 (2001) 727-745.
- [42] A. Pardo, M.C. Merino, A.E. Coy, F. Viejo, R. Arrabal, E. Matykina, Pitting corrosion behaviour of austenitic stainless steels – combining effects of Mn and Mo additions, *Corros. Sci.*, 50 (2008) 1796-1806.
- [43] C. Mapelli, D. Mombelli, A. Gruttadauria, S. Barella, E.M. Castrodeza, Performance of stainless steel foams produced by infiltration casting techniques, *J. Mater. Process. Technol.*, 213 (2013) 1846-1854.